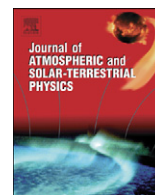




Contents lists available at ScienceDirect

Journal of Atmospheric and Solar-Terrestrial Physics

journal homepage: www.elsevier.com/locate/jastp

The thermospheric semiannual density response to solar EUV heating

Bruce R. Bowman^{a,*}, W. Kent Tobiska^{b,1}, Michael J. Kendra^{c,2}^a Air Force Space Command, AFSPC/A9AC, 250 S. Peterson Blvd, Ste 116, Peterson AFB, CO 80914, USA^b Space Environment Technologies, 1676 Palisades Dr., Pacific Palisades, CA 90272, USA^c Air Force Research Laboratory, AFRL/RVBYB, 29 Randolph Road, Hanscom AFB, MA 01731-3010, USA

ARTICLE INFO

Article history:

Received 8 January 2008

Received in revised form

3 April 2008

Accepted 18 April 2008

Keywords:

Thermosphere

Solar EUV

Neutral density

Semiannual variation

ABSTRACT

The goal of this study was to characterize the thermospheric semiannual density response to solar heating during the last 35 years. Historical radar observational data have been processed with special orbit perturbations on 28 satellites with perigee heights ranging from 200 to 1100 km. Approximately 225,000 very accurate average daily density values at perigee have been obtained for all satellites using orbit energy dissipation rates. The semiannual variation has been found to be extremely variable from year to year. The magnitude of the maximum yearly difference, from the July minimum to the October maximum, is used to characterize the yearly semiannual variability. It has been found that this maximum difference can vary by as much as 100% from one year to the next. A high correlation has been found between this maximum difference and solar EUV data. The semiannual variation for each year has been characterized based on analyses of annual and semiannual cycles, using Fourier analysis, and equations have been developed to characterize this yearly variability. The use of new solar indices in the EUV and FUV wavelengths is shown to very accurately describe the semiannual July minimum phase shifting and the variations in the observed yearly semiannual amplitude.

Published by Elsevier Ltd.

1. Introduction

The semiannual density variation was first discovered in 1961 (Paetzold and Zschorner, 1961). Paetzold and Zschorner observed a global density variation from analysis of satellite drag data, which showed a 6-month periodicity maximum occurring in April and October, and minimum occurring in January and July. Many authors, such as King-Hele and Hingston (1968), Cook (1969), and

Jacchia (1966, 1971a, 1977), analyzed the semiannual effect from satellite drag during the 1960s and early 1970s. They found that the semiannual variation was a worldwide effect, with the times of the yearly maximum and minimum occurring independent of height. However, the semiannual period was found to be only approximate, as the times of occurrence of the minima and maxima seemed to vary from year to year. Generally the October maximum exceeded that in April and the July minimum was deeper than that in January. The main driving mechanism for the observed variability in the semiannual effect remained a mystery. In his 1970 model Jacchia first modeled the effect as a temperature variation which included a function of the 81-day solar flux \bar{F}_{10} index. However, he soon discovered difficulties with the temperature model, and eventually modeled the semiannual variation as a density variation for his 1971 and 1977

* Corresponding author at: Air Force Space Command, Space Analysis, Colorado Springs, CO 80914, USA. Tel.: +1 719 556 3710.

E-mail addresses: bruce.bowman@peterson.af.mil (B.R. Bowman), ktobiska@spacenvironment.net (W. Kent Tobiska), michael.kendra@hanscom.af.mil (M.J. Kendra).

¹ Tel.: +310 573 4185 (office); fax: +310 454 9665 (fax).

² Tel.: +781 377 3203.

Report Documentation Page				Form Approved OMB No. 0704-0188	
Public reporting burden for the collection of information is estimated to average 1 hour per response, including the time for reviewing instructions, searching existing data sources, gathering and maintaining the data needed, and completing and reviewing the collection of information. Send comments regarding this burden estimate or any other aspect of this collection of information, including suggestions for reducing this burden, to Washington Headquarters Services, Directorate for Information Operations and Reports, 1215 Jefferson Davis Highway, Suite 1204, Arlington VA 22202-4302. Respondents should be aware that notwithstanding any other provision of law, no person shall be subject to a penalty for failing to comply with a collection of information if it does not display a currently valid OMB control number.					
1. REPORT DATE 2008		2. REPORT TYPE		3. DATES COVERED 00-00-2008 to 00-00-2008	
4. TITLE AND SUBTITLE The Thermospheric Semiannual Density Response to Solar EUV Heating				5a. CONTRACT NUMBER	
				5b. GRANT NUMBER	
				5c. PROGRAM ELEMENT NUMBER	
6. AUTHOR(S)				5d. PROJECT NUMBER	
				5e. TASK NUMBER	
				5f. WORK UNIT NUMBER	
7. PERFORMING ORGANIZATION NAME(S) AND ADDRESS(ES) Air Force Space Command,AFSPC/A9AC,250 S. Peterson Blvd, Ste 116,Peterson AFB,CO,80914				8. PERFORMING ORGANIZATION REPORT NUMBER	
9. SPONSORING/MONITORING AGENCY NAME(S) AND ADDRESS(ES)				10. SPONSOR/MONITOR'S ACRONYM(S)	
				11. SPONSOR/MONITOR'S REPORT NUMBER(S)	
12. DISTRIBUTION/AVAILABILITY STATEMENT Approved for public release; distribution unlimited					
13. SUPPLEMENTARY NOTES					
14. ABSTRACT The goal of this study was to characterize the thermospheric semiannual density response to solar heating during the last 35 years. Historical radar observational data have been processed with special orbit perturbations on 28 satellites with perigee heights ranging from 200 to 1100 km. Approximately 225,000 very accurate average daily density values at perigee have been obtained for all satellites using orbit energy dissipation rates. The semiannual variation has been found to be extremely variable from year to year. The magnitude of the maximum yearly difference, from the July minimum to the October maximum, is used to characterize the yearly semiannual variability. It has been found that this maximum difference can vary by as much as 100% from one year to the next. A high correlation has been found between this maximum difference and solar EUV data. The semiannual variation for each year has been characterized based on analyses of annual and semiannual cycles, using Fourier analysis, and equations have been developed to characterize this yearly variability. The use of new solar indices in the EUV and FUV wavelengths is shown to very accurately describe the semiannual July minimum phase shifting and the variations in the observed yearly semiannual amplitude.					
15. SUBJECT TERMS					
16. SECURITY CLASSIFICATION OF:			17. LIMITATION OF ABSTRACT Same as Report (SAR)	18. NUMBER OF PAGES 15	19a. NAME OF RESPONSIBLE PERSON
a. REPORT unclassified	b. ABSTRACT unclassified	c. THIS PAGE unclassified			

models. He also dropped the \bar{F}_{10} dependence, suggesting that he did not have enough data to support this solar flux relationship. He found that the amplitude of the semi-annual density variation was strongly height-dependent and variable from year to year. However, he could not show a definitive correlation of the variation with solar activity. All these previous analyses were limited to a relatively short time interval of a few years. More recent studies (Boulton, 1987; Sehnaal et al., 1988; Tawadrous, 1989) have combined several years of satellite drag data to analyze the semiannual variation, thus again missing the year-to-year variability. The purpose of this current study was to extend the previous study (Bowman, 2004b) to quantify the year-to-year variation over the last solar cycle using additional solar indices, and to show the semiannual density response to solar ultraviolet heating.

2. Data reduction

Daily temperature corrections to the US Air Force High Accuracy Satellite Drag Model's (HASDM) (Storz et al., 2002; Bowman and Storz, 2002) modified Jacchia 1970 atmospheric model have been obtained on 28 satellites during the period 1969–2006. Approximately 225,000 daily temperature values were obtained using a special energy dissipation rate (EDR) method (Bowman et al., 2004a), where radar and optical observations are fit with special orbit perturbations. For each satellite tracked from

1969 through 2000, approximately 100,000 total radar and optical observations were available for special perturbation orbit fitting. After year 2000 more than 50,000 observations per year were obtained for each satellite. A differential orbit correction program was used to fit the observations to obtain the standard 6 Keplerian elements plus the ballistic coefficient. “True” ballistic coefficients (Bowman, 2002) were then used, with the observed daily temperature corrections to obtain daily density values for different reference heights (average perigee heights). The daily density computation was validated (Bowman et al., 2004) by comparing historical daily density values computed for the last 30 years for over 30 satellites. The accuracy of the density values was determined from comparisons of geographically overlapping perigee location data, with over 8500 pairs of density values used in the comparisons. The daily density errors were found to be less than 4% overall, with errors on the order of 2% for values covering the latest solar maximum. The latter decrease in error is largely due to increased observation rates.

Table 1 lists all the satellites used for this study. A variety of orbit inclinations, from low to high, were used. The satellites with perigee heights below 600 km are in moderate to high eccentric orbits with apogee heights varying from 1500 to 20,000 km. The majority of the satellites are spheres, which avoids the possibility of frontal area problems producing invalid drag results. The first phase of the analysis used only the 81-day centered

Table 1
Satellites used for the semiannual density variation study

NORAD no.	INTL design	Type	Shape	True B (m ² /kg)	INCL (deg)	Apogee ht (km)	Perigee ht (km)	Start year	End year
26692	2001–004C	PAM-D R/B	Spheroid	0.02226	38.8	20,000	175	2001	2003
25935	1999–055 C	PAM-D R/B	Spheroid	0.02145	38.8	20,000	190	2001	2006
26362	2000–025 C	PAM-D R/B	Spheroid	0.02221	38.9	20,000	200	2005	2006
22781	1993–054 C	PAM-D R/B	Spheroid	0.02272	34.7	20,000	215	2000	2006
06073	1972–023 E	Venus Lander	Spheroid	0.00356	52.1	9800	220	1973	2006
22277	1992–089 C	PAM-D R/B	Spheroid	0.02237	34.9	20,000	240	1994	2006
04053	1969–064 C	Intelsat	Cylinder	0.00582	30.2	5400	265	1971	2006
14694	1964–011F	R/B	Cylinder	0.00196	27.7	1200	280	1984	2006
13985	1983–030 B	R/B	Cylinder	0.01851	25.3	4020	290	1983	2000
08063	1975–072 B	R/B	Cylinder	0.01946	89.2	2450	320	1979	2006
06895	1973–078 C	R/B	Cylinder	0.01745	28.8	2320	350	1974	1995
02150	1986–034A	OV3-1	Cylinder	0.01998	82.4	3750	360	2005	2006
02389	1986–070A	OV3-3	Cylinder	0.01796	81.4	2900	370	2005	2006
12388	1981–033A	RadarCal	Sphere	0.01121	83.0	1525	405	1982	2006
14483	1983–111A	RadarCal	Sphere	0.01121	82.9	1650	405	2000	2006
04382	1970–034A	DFH-1	Spheroid	0.01105	68.4	2125	450	1979	2006
10517	1977–118B	R/B	Cylinder	0.01871	28.7	1800	480	1980	2006
03827	1969–025 E	OV1-19 R/B	Cylinder	0.02289	104.8	5450	500	1969	2006
00022	1959–009A	Explorer 7	Dele cone	0.02297	50.3	810	510	2006	2006
00011	1959–001A	Vanguard 2	Sphere	0.05039	32.9	3000	560	1969	2006
00045	1960–007A	Transit 2A	Sphere	0.01615	66.7	975	625	1969	2006
01583	1965–072 D	R/B	Cylinder	0.04485	98.1	1050	640	2000	2006
01738	1985–093A	Explorer 30	Sphere	0.01572	59.7	850	700	1969	2006
02909	1987–053 J	Calsphere	Sphere	0.19578	70.0	750	750	1979	2006
05398	1971–067E	Rigid sphere 2	Sphere	0.06098	87.6	850	775	1972	2006
02826	1967–053A	Calsphere	Sphere	0.19279	69.9	900	850	1969	2006
00900	1964–063 C	Calsphere 1	Sphere	0.24239	90.2	1050	1025	1969	2006
01520	1965–065 H	Calsphere 4	Sphere	0.06994	90.1	1180	1100	1969	2006

The table is sorted by perigee height (in bold). The start and end years for the time span used in the data analysis are listed. The satellites highlighted by bold were used in the first phase of the analysis, while those highlighted by italics were added for the new solar indices phase.

average \bar{F}_{10} index, with the 13 satellites highlighted in bold in Table 1. The remaining satellites (highlighted in italics) were added along with new solar indices for the second phase of the analysis covering the 1997–2006 period.

The semiannual variations were computed first by differencing the computed daily density values with density values obtained from the HASDM modified Jacchia atmospheric model without applying Jacchia's semiannual equations. If Jacchia's model were perfect, then the resulting differences would only contain the observed semiannual variation. This is equivalent to computing the

“Density Index” D that has previously been used (Walker, 1978) to compute the semiannual variation. Figs. 1 and 2 show examples of the individual density differences obtained from the data. Also shown is the Jacchia semiannual density variation, and a Fourier series fitted to the smoothed density difference values. This Fourier function is discussed in detail below. As can be observed in the two figures, there is a very large unmodeled 27-day variation in the difference values. This results from Jacchia's model inadequately modeling the 27-day solar EUV effects (Bowman and Tobiska, 2006). Because of the very large 27-day variations in the data, it was decided to

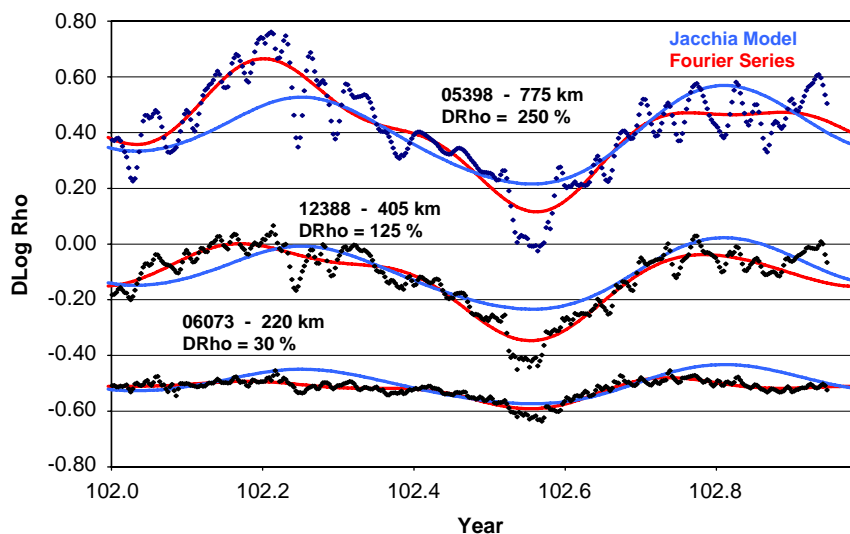


Fig. 1. Semiannual density variations for 2002 for selected satellites are plotted. Individual points are daily density difference values. Jacchia's model and individual satellite Fourier fits are also shown. The top and bottom set of curves have been offset in $D \log Rho (\Delta \log_{10} \rho)$ by +0.5 and -0.5, respectively, for clarity.

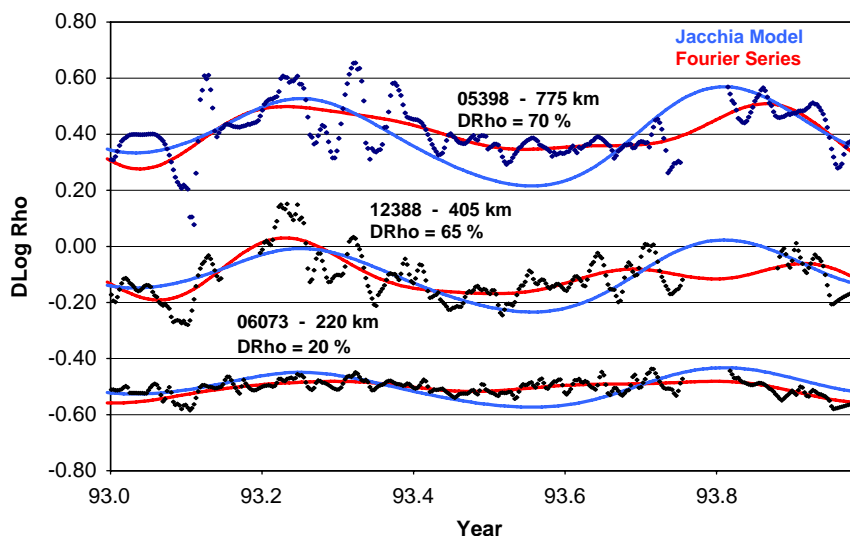


Fig. 2. Semiannual density variations for 1993 for selected satellites are plotted. Amplitudes of the semiannual variation are also shown as percent density changes. The top and bottom set of curves have been offset in $D \log Rho (\Delta \log_{10} \rho)$ by +0.5 and -0.5, respectively, for clarity.

smooth the values with a 28-day moving filter. The resulting values were then used to produce a smoother fit with the Fourier series.

It is interesting to note how the semiannual variation changes with height and time. Fig. 1 shows the variation during a year near solar maximum (2002), while Fig. 2 shows the variation during a solar minimum year (1993). The semiannual amplitude is measured from the yearly minimum, normally occurring in July, to the yearly maximum, normally in October. During solar maximum, the semiannual variation can be as small as 30% at 220 km, and as high as 250% near 800 km. During solar minimum, the maximum variation near 800 km is only 70% as shown in Fig. 2. Thus, there is a major difference in amplitudes of the yearly variation from solar minimum to solar maximum, unlike Jacchia's model, which maintains constant amplitude from year to year. This is discussed in detail below.

3. Semiannual density variation function

Initially Jacchia (1966) represented the semiannual density variation as strictly a temperature change. However, many difficulties arose from this that could not be explained in temperature space; so, to remove these difficulties, Jacchia eventually assumed that the semiannual variation was not caused by temperature, but by direct density variations. From Jacchia's analysis of 12 years of satellite drag data (Jacchia, 1971a, b, 1977) he obtained the following equations. Jacchia represented the semiannual density variation in the form

$$\Delta_{SA} \log_{10} \rho = F(z)G(t) \quad (1)$$

$G(t)$ represents the average density variation as a function of time in which the amplitude (i.e. the difference in \log_{10} density between the principal minimum in July and the principal maximum in October) is normalized to 1, and $F(z)$ is the relation between the amplitude and the height z .

In this study it was determined that a Fourier series could accurately represent Jacchia's $G(t)$ equation structure. It was determined that a 9-coefficient series, including frequencies up to 4 cycles per year, was sufficient to capture all the variability in $G(t)$ that had been previously observed by Jacchia and others (Sehnal et al., 1988).

It was also determined that a simplified quadratic polynomial equation in z could sufficiently capture Jacchia's $F(z)$ equation and not lose any fidelity in the observed $F(z)$ values.

The resulting equations used for the initial phase of this study were:

$$F(z) = B_1 + B_2 z + B_3 z^2 \quad (z \text{ in km}) \quad (2)$$

$$\begin{aligned} G(t) = & C_1 + C_2 \sin(\omega) + C_3 \cos(\omega) + C_4 \sin(2\omega) \\ & + C_5 \cos(2\omega) + C_6 \sin(3\omega) + C_7 \cos(3\omega) \\ & + C_8 \sin(4\omega) + C_9 \cos(4\omega) \end{aligned} \quad (3)$$

where

$$\omega = 2\pi\theta, \quad \theta = (t - 1.0)/365, \quad t = \text{year day} \quad (4)$$

The B and C equation coefficients above were fitted on a yearly basis using linear least squares.

3.1. Semiannual $F(z)$ height function

The amplitude, $F(z)$, of the semiannual variation was determined on a year-by-year and satellite-by-satellite basis. The smoothed density difference data were fit each year for each satellite using the 9-term Fourier series. The $F(z)$ value was then computed from each fit as the difference between the minimum and maximum values.

Fig. 3 shows the results of three different years of data, along with the plot of Jacchia's 1977 model $F(z)$ equation. For each year, the $F(z)$ values were fit with a quadratic polynomial in height. The smoothed curves shown in Fig. 3 represent the least squares quadratic fit obtained for three different years. The $\Delta \log_{10} \rho$ data for all satellites are very consistent within each year, producing a standard deviation of only $0.03 \Delta \log_{10} \rho$. The most notable item in Fig. 3 is the very large difference in maximum amplitude among the years displayed. The 2002 data show a maximum density variation of 250% near 800 km, while the 1993 data show only a 60% maximum variation. Jacchia's $F(z)$ function only gives a constant 130% maximum variation for all years. Fig. 4 shows the quadratic fits from solar minimum year 1993 through solar maximum year 2001. The year-to-year amplitude changes are readily apparent, with the greatest differences occurring during solar maximum.

From analysis of data during the 1960s and early 1970s, Jacchia found no noticeable variation in $F(z)$ with respect to solar activity. However, this study used over 35 years of data covering three separate solar cycles; so the next step was to correlate the $F(z)$ values with the 81-day centered average \bar{F}_{10} value.

To obtain a global fit, covering all years and all heights, all $F(z)$ values for all satellites and all years were fitted to obtain the $F(z)$ global model using the following equation:

$$F(z) = B_1 + B_2 z + B_3 z^2 + \bar{F}_Y (B_4 + B_5 z + B_6 z^2) \quad (5)$$

where z = (perigee height in km), and \bar{F}_Y is the yearly average of F_{10} .

The yearly average value of F_{10} was used because the amplitude of the semiannual variation is the difference of densities between the July minimum and the October maximum. The B coefficients were computed from linear least squares using all the observable semiannual amplitudes at different perigee heights covering the period 1969–2002. The yearly maximum global $F(z)$ values, occurring between 700 and 800 km, were then computed from Eq. (5).

Fig. 5 shows the observed yearly maximum $F(z)$ values and the fitted \bar{F}_Y global model maximum values plotted as a function of date. Also shown are the 81-day centered average \bar{F}_{10} values. The strong correlation of the yearly maximum $F(z)$ values with \bar{F}_{10} is readily apparent. Also apparent are the occasional more variable years (i.e. 1988, 1993, and 2002) that appear to occur less than 10% of the time. The second phase of the study was to determine if these larger amplitude excursions from the \bar{F}_Y global

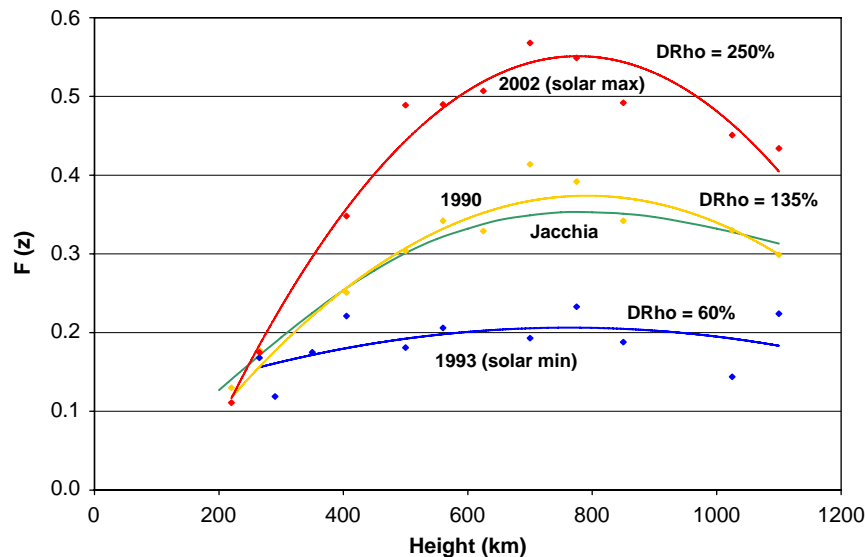


Fig. 3. The amplitude function $F(z)$ for three different years (1990, 1993, 2002), with semiannual amplitudes plotted for each satellite for each year. The constant $F(z)$ function from Jacchia is also plotted. The $F(z)$ for individual satellites at different perigee heights are shown as colored diamonds.

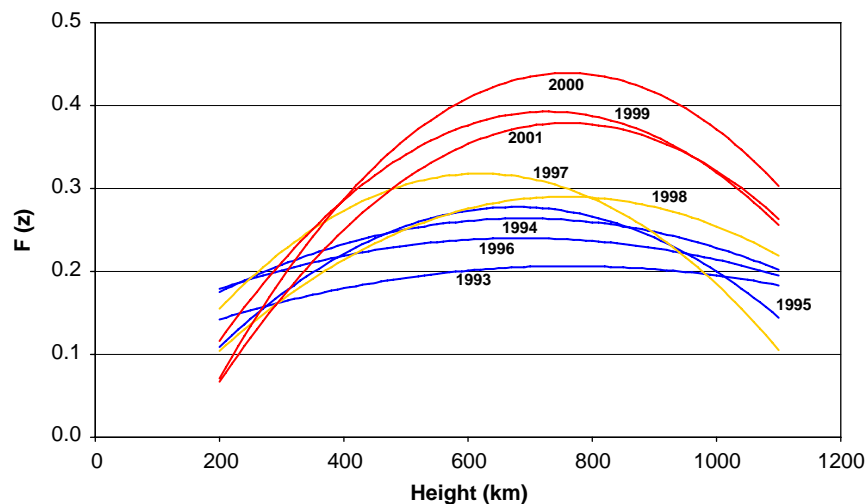


Fig. 4. The fitted $F(z)$ curves for solar minimum (1993) through solar maximum (2001). Solar minimum years are in blue, solar mid years are in yellow, and solar maximum years are in red.

model could be captured using solar heating expressed by using additional long-term EUV and FUV solar indices.

For this second phase the solar UV absorption in the thermosphere was analyzed. Fig. 6 is a plot of the thermospheric altitude at which the maximum absorption rate of solar UV radiation occurs as a function of wavelength (Jursa, 1985). The solar index F_{10} is really a proxy index because it is measured at a 10.7-cm wavelength, which is not a direct measure of any ultraviolet radiation. Direct ultraviolet heating indices were recently developed (Bowman and Tobiska, 2006) that represent the extreme (EUV), far (FUV), and mid (MUV) solar UV radiation. Fig. 6 shows that the maximum EUV heating occurs in the lower thermosphere at altitudes from 150 to 170 km. However, also apparently important

is the maximum heating near 120 km occurring in the FUV region. This indicates that at least one EUV and one FUV solar index should be required to capture the thermospheric heating from solar irradiance.

Roble (1987) computed the thermospheric temperature response to solar EUV heating using his coupled thermosphere and ionosphere global average model. Fig. 7 shows the decrease in temperature that would occur from removing specific EUV solar heating wavelengths. Removing the He II 30.4 nm emission produced the largest (by a factor of 2) temperature change. Therefore, it was very important to select an EUV index that captured the emission of this He II irradiance line. These results together with previous analysis (Bowman and Tobiska, 2006) of thermospheric response to new solar indices

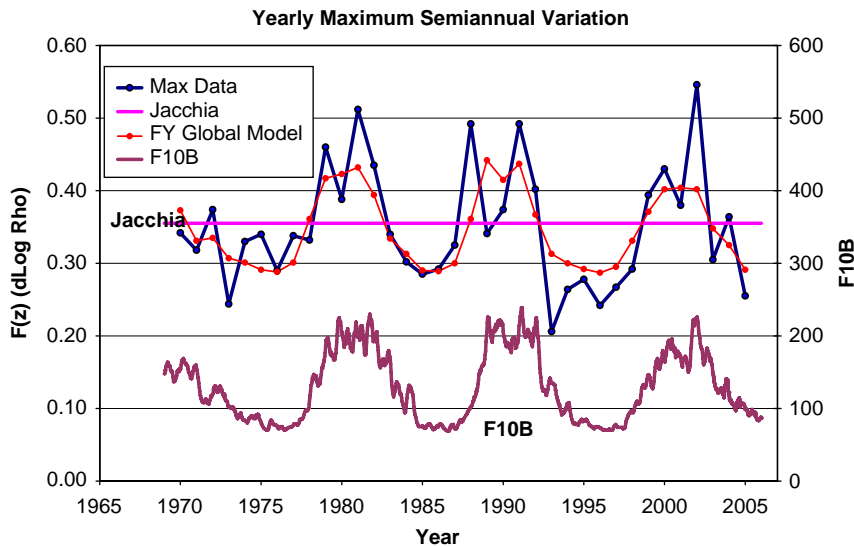


Fig. 5. The observed maximum $F(z)$ value for each year plotted by year. Also shown are the computed maximum $F(z)$ values using the \bar{F}_Y (FY) global model. The 81-day F_{10} average, F10B, is displayed, along with Jacchia's constant maximum amplitude value.

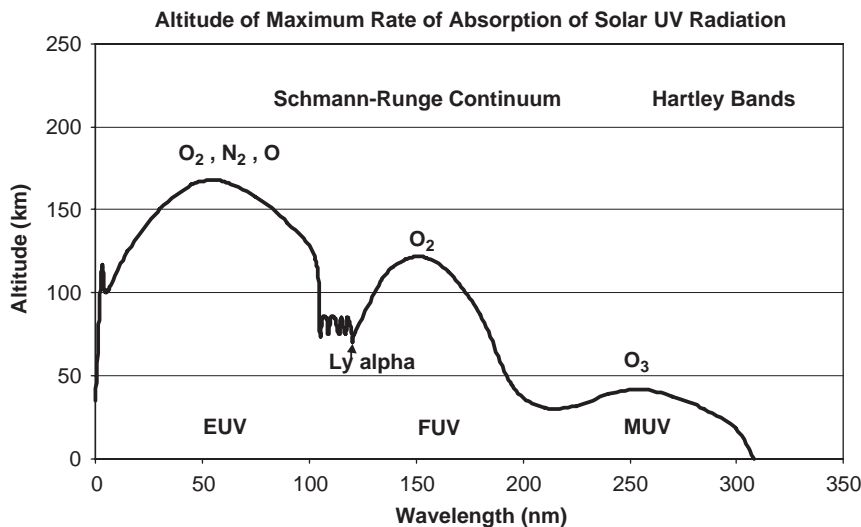


Fig. 6. The altitude is shown for the maximum rate of absorption of solar ultraviolet radiation as a function of solar spectrum wavelength. EUV—extreme ultraviolet, FUV—far ultraviolet, and MUV—mid ultraviolet region. The relevant atomic/molecular species for absorption is also listed.

suggested a new set of solar indices to use for this second phase of the study. New 81-day centered values were computed for use along with the previous \bar{F}_{10} index. These new indices were \bar{S}_{10} , \bar{M}_{10} , and \bar{E}_{SRC} , which are defined as given below:

S_{10} : The NASA/ESA Solar and Heliospheric Observatory (SOHO) research satellite operates in a halo orbit at the Lagrange Point 1 (L1) on the Earth–Sun line, approximately 1.5 million km from the Earth. One of the instruments on SOHO is the solar extreme-ultraviolet monitor (SEM), which has been measuring the 26–34 nm solar EUV emission since launch in December 1995. This integrated 26–34 nm emission has been normalized and converted to sfu through linear regression with F_{10} , producing the new

index S_{10} . The broadband (wavelength integrated) SEM 26–34 nm irradiances are EUV line emissions dominated by the chromospheric He II line at 30.4 nm with contributions from other chromospheric and coronal lines. This energy principally comes from solar active regions. \bar{S}_{10} is the 81-day centered average of S_{10} .

Mg_{10} : The NOAA series of operational satellites, e.g., NOAA 16 and NOAA 17, host the solar backscatter ultraviolet (SBUV) spectrometer, which has the objective of monitoring ozone in the Earth's lower atmosphere. In its discrete operating mode, a diffuser screen is placed in front of the instrument's aperture in order to scatter solar MUV radiation near 280 nm into the instrument. This solar spectral region contains both photospheric

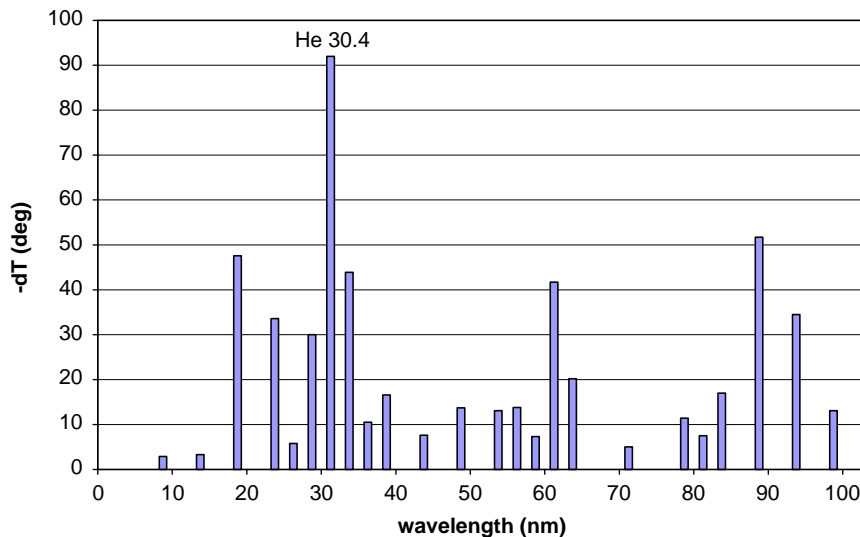


Fig. 7. Thermospheric temperature sensitivity to solar EUV irradiances. Negative thermospheric temperature changes ($-dT$) are displayed resulting from removal of selected solar irradiance wavelengths.

continuum and chromospheric line emissions. The chromospheric Mg II *h* and *k* lines at 279.56 and 280.27 nm, respectively, and the weakly varying photospheric wings (or continuum longward and shortward of the core line emission), are operationally observed by the instrument. The Mg II core-to-wing ratio (cwr) is calculated between the variable lines and nearly non-varying wings. The result is a measure of chromospheric and some photospheric solar active region activity independent of instrument sensitivity change through time, and is referred to as the Mg II cwr, which is provided daily by the NOAA Space Environment Center (SEC) (Viereck et al., 2001). The Mg II cwr has been used in a linear regression with F_{10} to derive the M_{10} index in sfu units. \bar{M}_{10} is the 81-day centered average of M_{10} .

E_{SRC} : The solar FUV Schumann–Runge continuum (SRC) contains emission between 125–175 nm from the photosphere and lower chromosphere. This solar energy is deposited in the terrestrial mesosphere and lower thermosphere (80–125 km) primarily through the energy released from the dissociation of molecular oxygen. The SRC has been observed by the SOLSTICE instrument on the UARS (Rottman and Woods, 1994) and SORCE (McClintock et al., 2000) NASA research satellites, as well as by the SEE instrument on NASA TIMED research satellite (Woods et al., 1994). We have selected the 145–165 nm band as a representative wavelength range of the SRC since the emission in this band is mostly deposited in the 110–125 km altitude region. For our analysis, we have integrated the daily SOLSTICE 145–165 nm emission and then performed a linear regression with F_{10} to report the index E_{SRC} , in sfu. \bar{E}_{SRC} is the 81-day centered average of E_{SRC} .

Since the first phase of the study showed a high correlation of the \bar{F}_{10} 81-day average values with the yearly semiannual amplitudes, it was decided to continue the study by adding the solar flux from the long-term EUV

\bar{S}_{10} index and the long-term \bar{M}_{10} representing the FUV heating. It was decided to combine the indices in a linear function since each index is expressed in terms of F_{10} units and this approach (Bowman and Tobiska, 2006) previously worked very well in defining a new exospheric temperature equation as a function of solar heating. Irradiance data for developing these new indices were available since 1997; so this analysis used the observed semiannual variations from 1997 through 2006. The previously derived (Bowman and Tobiska, 2006) exospheric nighttime temperature equation was

$$T_c = 379.0 + 3.353\bar{F}_{10} + 0.358(F_{10} - \bar{F}_{10}) + 2.094(S_{10} - \bar{S}_{10}) + 0.343(M_{10} - \bar{M}_{10}) \quad (6)$$

After removing the constant and the daily indice terms, the new long-term temperature variation equation was

$$\Delta T_c = +2.995\bar{F}_{10} - 2.094\bar{S}_{10} - 0.343\bar{M}_{10} \quad (7)$$

A new index was then created from this equation by normalizing the coefficients by the \bar{F}_{10} coefficient to give

$$\bar{F}_{\text{SM}} = 1.00\bar{F}_{10} - 0.70\bar{S}_{10} - 0.115\bar{M}_{10} \quad (8)$$

In the previous analysis (Bowman and Tobiska, 2006), when using the different 81-day solar indices it was shown that the \bar{F}_{10} index was much better at representing the long-term 11-year solar cycle density variations than using either the \bar{S}_{10} or the \bar{M}_{10} index. This is reflected in the coefficients in Eqs. (7) and (8), which show that the contribution of the \bar{F}_{10} coefficient is larger than that from either of the other two coefficients. This implies that the irradiance from the solar cool corona, as measured by \bar{F}_{10} , is more significant for long-term density variations than the irradiance from the solar chromosphere, as measured by \bar{S}_{10} and \bar{M}_{10} . Eq. (8) was used as the initial starting point for obtaining the best fit solution for the coefficients representing the semiannual density variations. Since the

semiannual density amplitude is based on density difference values separated by 4–6 months during the year, it was decided to use a yearly average for the solar indices to correlate with the yearly amplitudes. This new semiannual density index was defined as

$$\bar{F}_{SMY} = A_1 \bar{F}_Y + A_2 \bar{S}_Y + A_3 \bar{M}_Y \quad (9)$$

where the \bar{F}_Y , \bar{S}_Y , and \bar{M}_Y indices represent the yearly averages of the F_{10} , S_{10} , and M_{10} indices, respectively. This \bar{F}_{SMY} index was then used to determine which terms were significant in defining a new $F(z)$ equation. The resultant new $F(z)$ equation, with $z = \text{height (km)}/1000$, using the new index was determined to be

$$F(z) = B_1 + B_2 \bar{F}_{SMY} + B_3 z \bar{F}_{SMY} + B_4 z^2 \bar{F}_{SMY} + B_5 z \bar{F}_{SMY}^2 \quad (10)$$

A non-linear least squares method was used for simultaneously determining the A coefficients in Eq. (9) and the B coefficients in Eq. (10), initially starting with values from Eq. (8). The A_1 value was fixed to 1.00 and the A_2 and A_3 values were fit simultaneously with the B coefficients in Eq. (10) to minimize the residuals between the observed yearly semiannual amplitude $F(z)$ values and the $F(z)$ Eq. (10) values. After the best solution was

obtained, it was also decided to try to use the indices as averaged values over just the month of July. This was done because the semiannual minimum occurs around the July time period, and this minimum value is a major part of defining the yearly amplitude value. These new indices, \bar{F}_J , \bar{S}_J , and \bar{M}_J , were then used as replacements of the \bar{F}_Y , \bar{S}_Y , and \bar{M}_Y indices in Eq. (9). The same method described above was then used to determine a new set of A and B coefficients. Final analysis of the yearly and July averaged $F(z)$ residuals showed that there was a slight improvement in reducing the $F(z)$ residuals using the July averaged values. Therefore, these July averaged indices were adopted for the rest of the $F(z)$ analysis.

The non-linear least squares minimum is broad for the solution of the \bar{S}_J and \bar{M}_J coefficients. Because of the relatively short data span of only one 11-year solar cycle, the \bar{S}_J and \bar{M}_J coefficients are highly correlated. The sum of these two coefficients appears to be ~ -0.74 , with the \bar{S}_J coefficient varying around the minimum between -0.63 and -0.75 . The resulting best fit new solar index to replace \bar{F}_{SMY} in Eq. (10) above was determined to be

$$\bar{F}_{SMJ} = 1.00 \bar{F}_J - 0.70 \bar{S}_J - 0.04 \bar{M}_J \quad (11)$$

The coefficient values in Eq. (11) are in good agreement with the values in Eq. (8) that were originally derived from the new Tc temperature equation.

Table 2 lists the resulting B coefficient values, with their standard deviations obtained from using Eq. (11) for the solar index in Eq. (10). The standard deviations of all the coefficients are an order of magnitude less than the coefficient values, indicating that all five coefficients have been well determined.

Eq. (10) using \bar{F}_{SMJ} represents a global equation in $F(z)$ using data from yearly semiannual amplitudes observed from 1997 through 2006. The results of using this model for year 2002 are labeled as the GLB (global) FSMB model in Fig. 8. The development of Eqs. (10) and (11) was

Table 2
 $F(z)$ coefficient values with standard deviations (STD) from best fit results

Coef.	Term	Value	STD
B_1	1	2.69E-01	1.84E-02
B_2	\bar{F}_{SMJ}	-1.18E-02	6.56E-04
B_3	$z \bar{F}_{SMJ}$	2.78E-02	1.92E-03
B_4	$z^2 \bar{F}_{SMJ}$	-2.78E-02	1.20E-03
B_5	$z \bar{F}_{SMJ}^2$	3.47E-04	3.51E-05

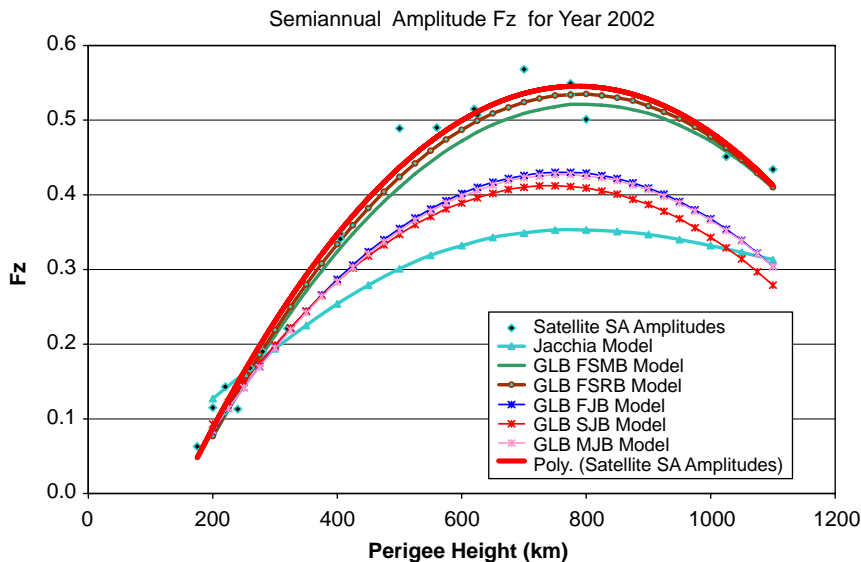


Fig. 8. Global model values for the 2002 semiannual density amplitudes for different satellite perigee altitudes (colored diamonds). The quadratic polynomial fit is also plotted.

repeated, but by replacing the \bar{F}_{SMJ} index with different solar indices to compare additional $F(z)$ global models. A new index, \bar{F}_{SRJ} , was computed based on replacing the \bar{M}_j index with the Schuman–Runge index \bar{E}_j based on the July average of the \bar{E}_{SRC} described above. This model is labeled as the GLB FSRB model in Fig. 8. Additional global models were then computed using only \bar{F}_j , \bar{S}_j and \bar{M}_j separately, and their results are labeled as GLB FJB, GLB SJB, and GLB MJB, respectively. Fig. 8 shows the results of all of these global models for 2002, comparing them with the 2002 semiannual amplitudes ($F(z)$) as a function of altitude. Year 2002 was chosen for the comparison plot because the observed amplitude is much larger than for any of the other years when solar indices are available, and for 2002 the $F(z)$ amplitude residuals from the previous 35-year F10B model are also the largest. All of the individual index global models \bar{F}_j , \bar{S}_j , and \bar{M}_j are very consistent among themselves, but all underestimate the amplitude for all altitudes. However, the individual index global models are still better than the constant Jacchia model, which really underestimates the amplitudes. The two global models representing a linear combination of the solar indices do very well at representing the large 2002 amplitudes. The \bar{F}_{SRJ} model using the Schumann–Runge index does the best, but using the \bar{F}_{SMJ} model with the Mg II cwr as a replacement for the real FUV heating is an excellent choice. Fig. 9 is a snapshot of Fig. 5 for 1997–2006. In Fig. 9 the original 35-year F10B global model is again compared with the yearly observed maximum of the semiannual amplitude, and the new global \bar{F}_{SMJ} model is compared for the years from 1997 through 2006. As can be seen in the figure, the multi-solar index model fits the observed maximum amplitudes much better throughout the entire time span than the single solar index F10B model.

3.2. Semiannual $G(T)$ yearly periodic function

The yearly observed $G(t)$ function, as previously discussed, consists of a Fourier series with 9 coefficients

representing a quadannual variation. The 28-day smoothed density difference data for each satellite were fitted with this Fourier series for each year. The density difference data are the accurate observed daily density values minus the Jacchia values without Jacchia's semi-annual variation. The $G(t)$ function was then obtained by normalizing to a value of 1 the difference between the minimum and maximum values for the year. The $F(z)$ value for each satellite by year was used for the normalization. Fig. 10 shows the results obtained for the year 1990 for the majority of the satellites. Note the tight consistency of the curves for all heights, covering over 800 km in altitude, which demonstrates the validity of using one $G(t)$ function per year to represent the yearly semiannual phase for all altitudes. This tight consistency of the $G(t)$ phase for all satellites also indicates that there is no apparent latitude or local solar time effects with the semiannual density variation. This conclusion can be made because the majority of the satellites have moderate to high eccentricity orbits, as is apparent from the perigee and apogee heights listed in Table 1. This means that the great majority of the density sampling on each revolution occurs very close to the perigee location, and the daily density values computed from the orbit decays can be assigned to the argument of perigee latitude and local solar time, which is different for each satellite. The precession of the argument of perigee can be very slow (from zero to a few degrees per day); so if there is a latitude or local solar time semiannual effect the $G(t)$ phase curves in Fig. 10 should show significant differences because of the random nature of the argument of perigee locations. This is definitely not observed when comparing all of the individual satellite $G(t)$ phase curves.

The next step in the study was to fit a yearly $G(t)$ function for each year using the data for all the satellites for the year. Fig. 10 also shows the yearly fit $G(t)$ value for the year 1990. A small standard deviation was obtained for every year's fit, especially during solar maximum

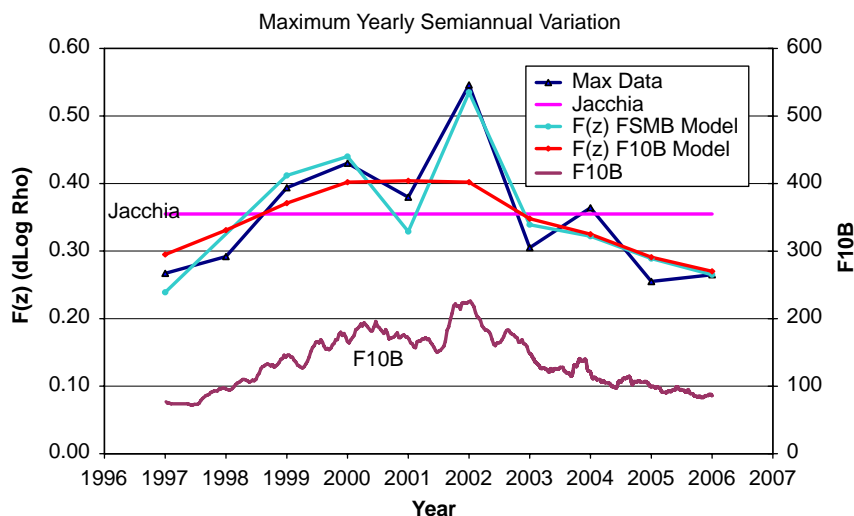


Fig. 9. The observed maximum $F(z)$ amplitude semiannual values for each year (Max data) are plotted by year. The older F10B global model and combined solar indices global model FSMB values are also plotted along with the F10B (\bar{F}_{10}) 81-day averaged solar index.

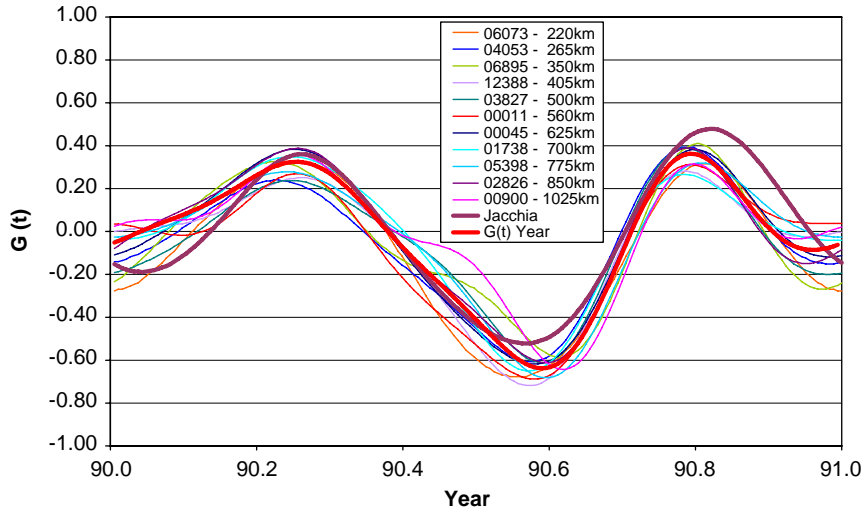


Fig. 10. The individual satellite $G(t)$ fits are plotted for 1990. The Jacchia model and yearly fit model are also shown.

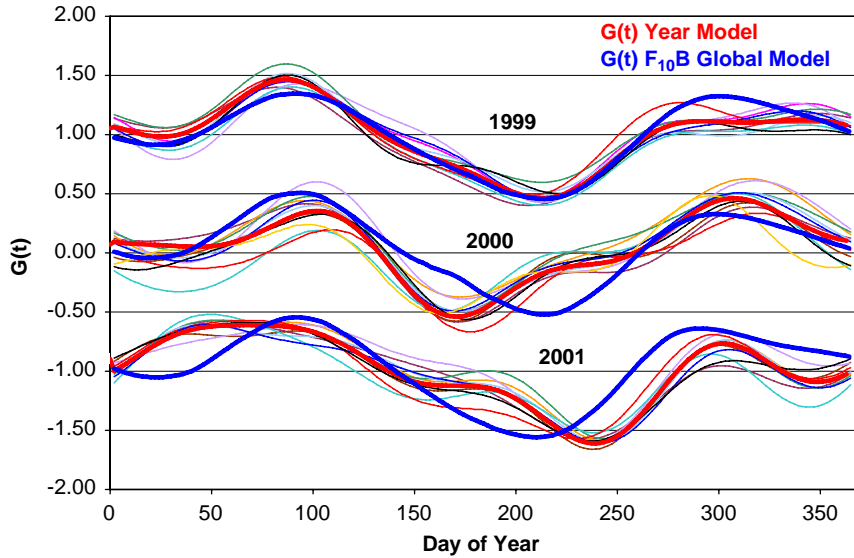


Fig. 11. The individual satellite fits for 3 different years are shown. The year $G(t)$ model is highlighted. Each set of curves for 1999 and 2001 has been offset by +1.00 and -1.00, respectively, in $G(t)$ for clarity. The 18-term global \bar{F}_{10} model curve is also displayed.

years. Fig. 11 shows the yearly $G(t)$ fits for 1999–2001, again showing the consistency of the semiannual phase at all altitudes for a given year. Also, it is readily apparent that the series changes dramatically from year to year. It was determined that during solar maximum the July minimum date can vary by as much as 80 days. During solar minimum the semiannual July minimum time variation is much smaller and appears to be flattened out in time.

A global $G(t)$ function was then obtained using all satellite data for all years from 1969 through 2002. Since the yearly $G(t)$ functions demonstrated a dependence on solar activity, it was decided to expand the series as a function of the 81-day centered average \bar{F}_{10} , initially using only a linear term in \bar{F}_{10} . The following 18-term

equation was adopted for the global $G(t)$ function:

$$G(t) = C_1 + C_2 \sin(\omega) + C_3 \cos(\omega) + C_4 \sin(2\omega) + C_5 \cos(2\omega) + C_6 \sin(3\omega) + C_7 \cos(3\omega) + C_8 \sin(4\omega) + C_9 \cos(4\omega) + \bar{F}_{10}\{C_{10} + C_{11} \sin(\omega) + C_{12} \cos(\omega) + C_{13} \sin(2\omega) + C_{14} \cos(2\omega) + C_{15} \sin(3\omega) + C_{16} \cos(3\omega) + C_{17} \sin(4\omega) + C_{18} \cos(4\omega)\} \quad (12)$$

The results of the least squares fit to determine the C coefficients in Eq. (12) are plotted in Fig. 11 for years 1999, 2000, and 2001. The global \bar{F}_{10} $G(t)$ equation captures the general character of the observed yearly $G(t)$ values, but does not account for the July minimum variation. Even adding (Bowman et al, 2006) additional quadratic \bar{F}_{10}^2

annual and semiannual terms to Eq. (12) did not capture the observed July variation. Adding additional solar heating to attempt to account for this variation was the next step in the study.

The next phase of the study was conducted using the new solar indices \bar{S}_{10} and \bar{M}_{10} . \bar{M}_{10} was chosen in place of the true FUV index \bar{E}_{SRC} because \bar{M}_{10} was more readily available from multiple satellite data, and because it had been previously demonstrated (Bowman and Tobiska, 2006) that the \bar{M}_{10} index was a very good substitute for the \bar{E}_{SRC} index. As was done for the $F(z)$ analysis, it was decided to combine the indices in a linear function since each index is expressed in terms of F_{10} units and this approach worked very well for the $F(z)$ analysis. A new solar index, representing long-term EUV and FUV heating, was defined as

$$\bar{F}_{\text{SM}} = D_1 \bar{F}_{10} + D_2 \bar{S}_{10} + D_3 \bar{M}_{10} \quad (13)$$

It was decided to start out using only annual and semiannual terms, instead of the quadannual terms previously used, to try to represent the yearly semiannual phase variations. The yearly observed values had been fit with terms up to quadannual, but it was hoped that only terms up to semiannual needed to be included for a global model. The resulting equation used for this part of the study was

$$G(t) = C_1 + C_2 \sin(\omega) + C_3 \cos(\omega) + C_4 \sin(2\omega) + C_5 \cos(2\omega) + \bar{F}_{\text{SM}} \{C_6 + C_7 \sin(\omega) + C_8 \cos(\omega) + C_9 \sin(2\omega) + C_{10} \cos(2\omega)\} \quad (14)$$

A non-linear least squares method was used for simultaneously determining the D coefficients in Eq. (13) and the C coefficients in Eq. (14). The D_1 value was set to 1.00 and the D_2 and D_3 values were fit simultaneously with the C coefficients in Eq. (14) to minimize the residuals between the observed yearly phase values and the Eq. (14) values. The resulting new solar index \bar{F}_{SM} was determined to be

$$\bar{F}_{\text{SM}} = 1.00 \bar{F}_{10} - 0.75 \bar{S}_{10} - 0.37 \bar{M}_{10} \quad (15)$$

The coefficients in Eq. (15) are better defined than those for the $F(z)$ index function specified by Eq. (11). This is because density ($G(t)$) data and \bar{F}_{SM} values were available throughout the entire year as opposed to using one July averaged value per year used to derive Eq. (11). The agreement between the coefficients from Eqs. (15), (11), and (8) is remarkable considering the derivations were using different data types and data frequencies.

Table 3 lists the resulting C coefficient values with their standard deviations obtained from using Eq. (15) for the solar index used in Eq. (14). The standard deviations of the coefficients are all an order of magnitude smaller than the coefficient values, except for the C_7 and C_8 \bar{F}_{SM} annual terms, indicating a well-determined set of coefficients.

The results of the new global model from Eqs. (14) and (15) are plotted in Fig. 12 as the FSMB model. Also plotted are the yearly observed values for each year, and the original \bar{F}_{10} (F10B) global model values. The years 2000–2002 were chosen for comparisons because of the large variability in the July minimum time and amplitude from year to year. The solar indices \bar{F}_{10} , \bar{S}_{10} , and \bar{M}_{10} are

Table 3

$G(t)$ coefficient values with standard deviations (STD) from the best fit results

Coef.	Term	Value	STD
C_1	1	$-3.63\text{E}-01$	$6.33\text{E}-03$
C_2	$\sin(\omega)$	$8.51\text{E}-02$	$9.23\text{E}-03$
C_3	$\cos(\omega)$	$2.40\text{E}-01$	$8.60\text{E}-03$
C_4	$\sin(2\omega)$	$-1.90\text{E}-01$	$8.61\text{E}-03$
C_5	$\cos(2\omega)$	$-2.55\text{E}-01$	$8.79\text{E}-03$
C_6	\bar{F}_{SM}	$-1.79\text{E}-02$	$3.63\text{E}-04$
C_7	$\bar{F}_{\text{SM}} \sin(\omega)$	$5.65\text{E}-04$	$5.39\text{E}-04$
C_8	$\bar{F}_{\text{SM}} \cos(\omega)$	$-6.41\text{E}-04$	$4.77\text{E}-04$
C_9	$\bar{F}_{\text{SM}} \sin(2\omega)$	$-3.42\text{E}-03$	$4.91\text{E}-04$
C_{10}	$\bar{F}_{\text{SM}} \cos(2\omega)$	$-1.25\text{E}-03$	$5.07\text{E}-04$

also plotted for each year. The 10-term new model results are impressive. Even with only annual and semiannual terms, the new model accounts almost completely for the July minimum phase shifting which could not be captured in the \bar{F}_{10} global model using even quadannual terms. This clearly demonstrates that the large majority of the variations observed in the semiannual density variation can be attributed to direct solar heating responses.

4. October maximum variations

The yearly observed semiannual maximum normally displays a typical smooth pattern peaking in October, with the October maximum usually somewhat higher than the April maximum, as shown in Fig. 10. However, there are several years when this pattern is not followed. Fig. 13 shows the normalized yearly $G(t)$ values for the years 1980, 1999, and 2003. During these years the 81-day centered solar values increase during October (shown in a box), while the semiannual response during these October maxima is noticeably suppressed. The global FSMB model captures part of this decrease for 1999 and 2003, but tends to overestimate the suppression in 2003. Fig. 14 compares FSMB and $G(t)$ for these years. The FSMB is usually negative and the predominantly negative coefficients involving this term, shown in Table 3, lead to a net positive contribution to $G(t)$. In October 1999 FSMB tends toward zero and in October 2003 it becomes slightly positive, accounting for the suppressed $G(t)$ values, and is in good agreement with $G(t)$ year values compared to $G(t)$ \bar{F}_{10} model results. The reason for the apparent inability of \bar{F}_{10} to adequately measure solar EUV variability during these times is unknown; so additional studies will have to be undertaken to explain this phenomenon.

5. Conclusions

The following results concerning the thermospheric semiannual density variation have been obtained from the current study:

1. The semiannual effect is worldwide, and within each year the maxima and minima occur at the same dates independent of latitude, local solar time, or altitude.

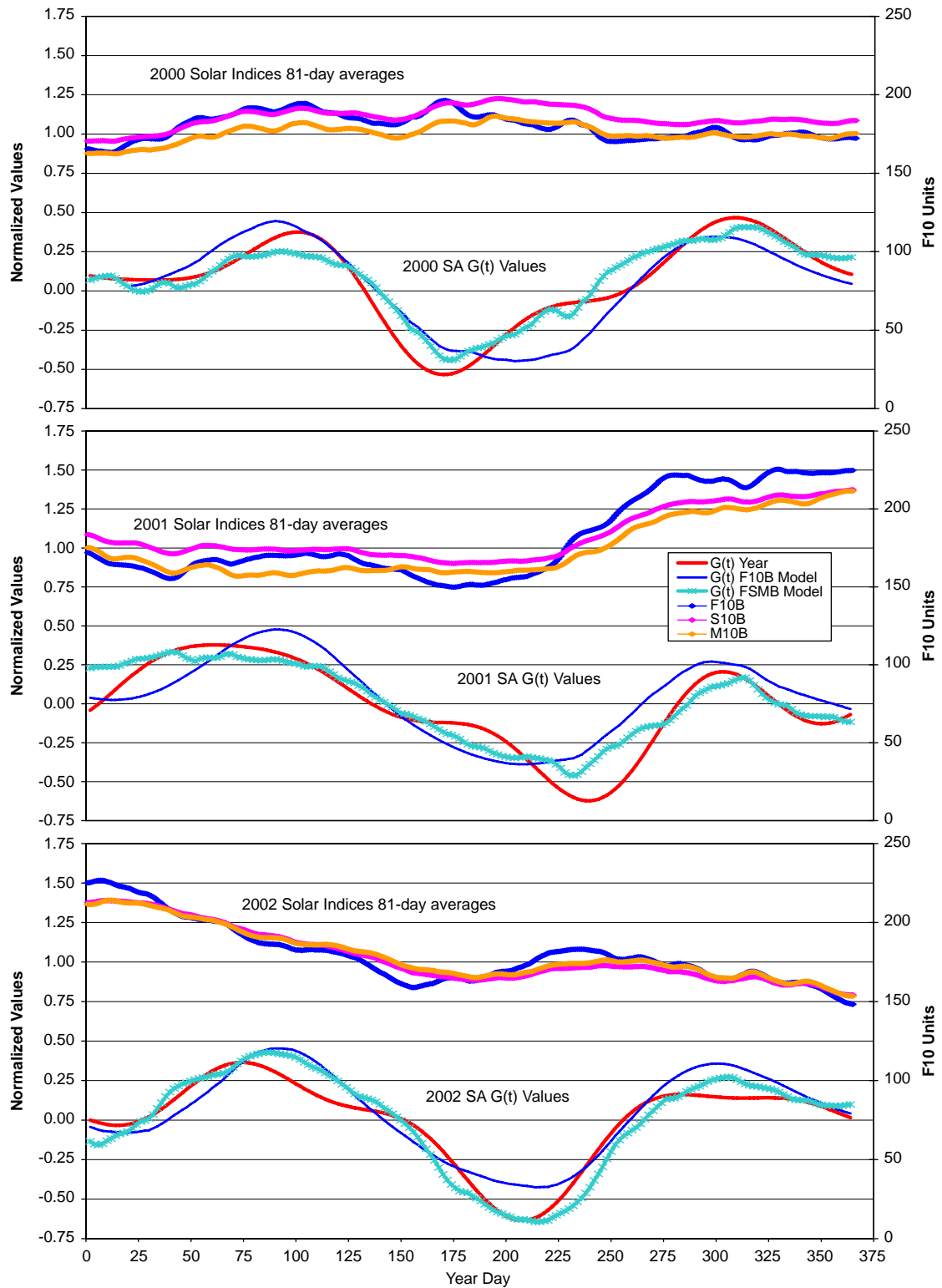


Fig. 12. Semiannual normalized $G(t)$ observed and modeled values for years 2000, 2001, and 2002 are shown. The individual 81-day averaged solar indices F_{10} , S_{10} , and M_{10} are also displayed for each of the years.

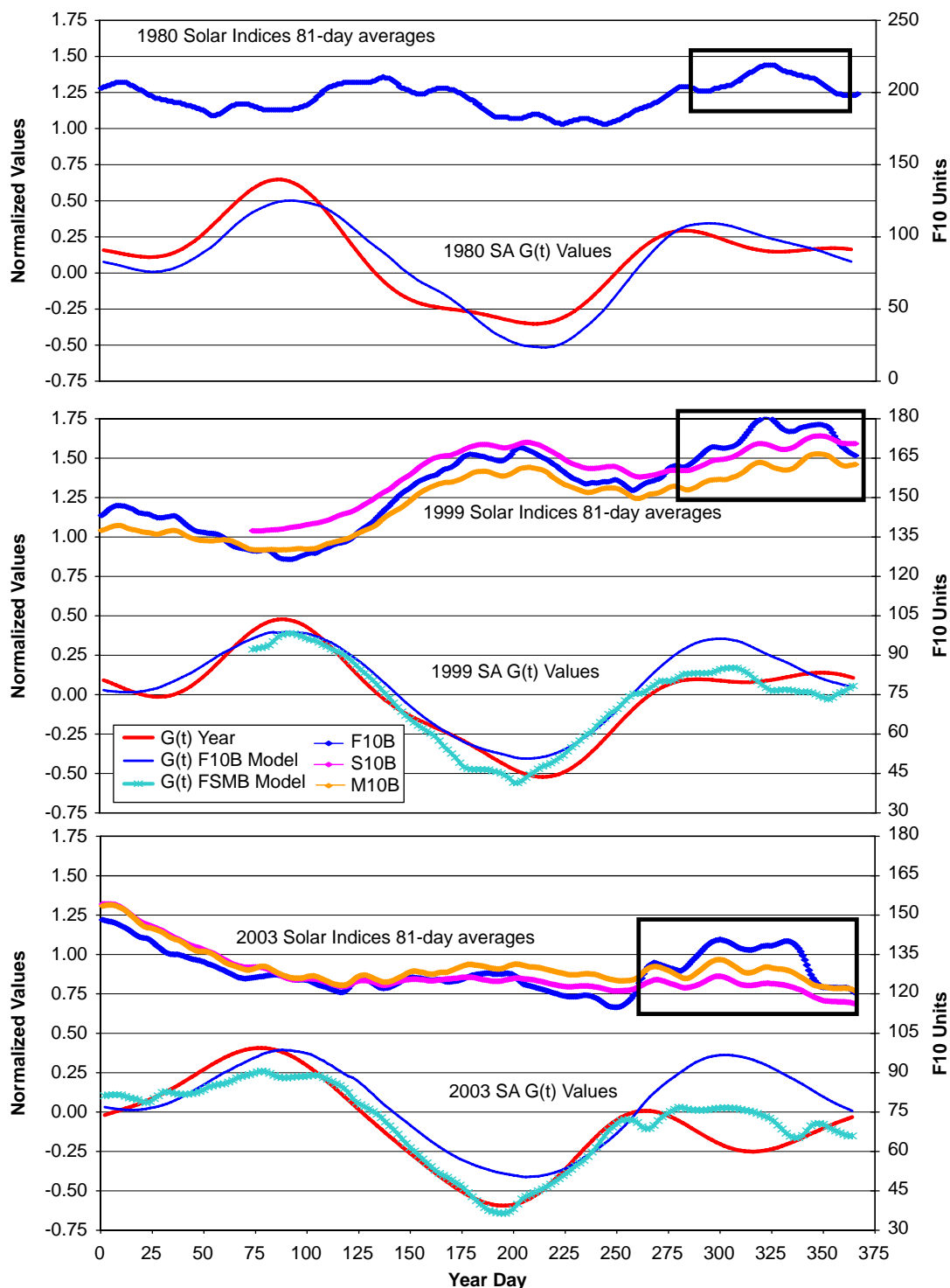


Fig. 13. Semiannual normalized $G(t)$ observed and modeled values for years 1980, 1999, and 2003 are shown. The individual 81-day averaged solar indices F_{10} , S_{10} , and M_{10} are also displayed for each of the years. The October increase in the 81-day average indices values is boxed in.

2. The yearly amplitude can change from year to year by 60% during solar minimum to over 250% during solar maximum.

3. The time span between the July minimum and the October maximum dates can vary by as much as 80 days, especially during solar maximum.

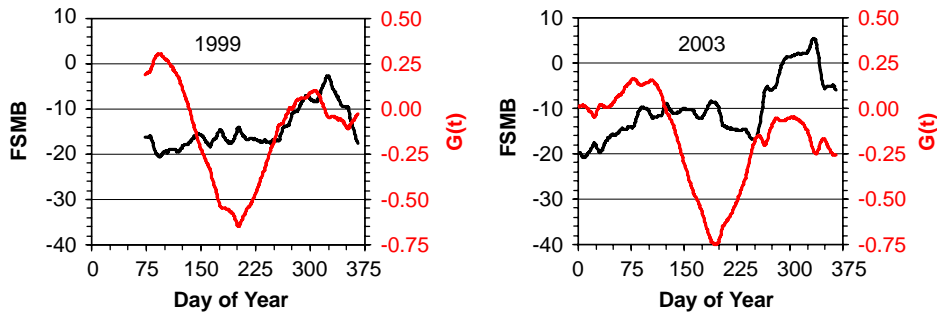


Fig. 14. $G(t)$ and FSMB index values for years 1999 and 2003 are plotted as a function of day of year. The red plots are the $G(t)$ values, while the black plots are for the FSMB (\bar{F}_{SM}) new solar index.

4. The yearly variation in amplitude and phase of the semiannual variation is highly correlated with solar activity.
5. A combination of solar EUV and FUV indices is required to accurately model the semiannual amplitude and phase variations observed from year to year.

The original \bar{F}_{10} model was unable to completely account for semiannual effect phase and amplitude variations, while the FSMB model representation does extremely well at modeling the variability. One possible reason is that \bar{F}_{10} includes both chromospheric and coronal sources, while \bar{S}_{10} and \bar{M}_{10} are primarily chromospheric. Given our finding that the majority of the semiannual variability is due to solar EUV and FUV changes, it then seems reasonable to assume that the coronal component over- or underestimates the variation at times using \bar{F}_{10} alone. As seen from Fig. 14, the \bar{S}_{10} and \bar{M}_{10} terms tend to compensate for this by adjusting FSMB accordingly.

A couple of the outstanding issues concerning the semiannual density variation are discovering the real physical source of the semiannual effect and explaining the remaining deviations from the current FSMB model. The remaining deviations could be a result of not capturing all the EUV and FUV heating with FSMB; so as more complete EUV and FUV data become available over the next solar cycle, this analysis needs to be redone with a full compliment of solar heating data. Discovering the real source of the semiannual effect will be more challenging. Fortunately, in conducting this research the measure of the real semiannual variation on a yearly basis has been obtained for the last several decades, which will provide the data needed to validate any physics-based semiannual model. These data, in terms of amplitude $F(z)$ and phase $G(t)$ yearly equations, are available upon request.

In conclusion, accurate yearly thermospheric semiannual density variations have been obtained for the period 1969–2006. The yearly variability response in the thermospheric semiannual density can be accurately captured by modeling EUV, FUV, and F_{10} cool corona solar heating.

Acknowledgments

The authors would like to thank Mark Storz (USAF/AFSPC) for his insight and valuable contributions toward

the theoretical development of the satellite drag data, and thanks to Tim Fuller-Rowell (NOAA/SEC) for his useful discussions and suggestions on the semiannual density variation theory.

References

- Boulton, W.J., 1987. The semi-annual variation in air density from June 1974 until September 1977 from the analysis of the orbit of Intercoms 10 Rocket (1973–82B). *Planetary and Space Science* 35, 1127.
- Bowman, B.R., 2002. True satellite ballistic coefficient determination for HASDM, AIAA 2002–4887. AIAA/AAS Astrodynamics Specialist Conference, Monterey, CA.
- Bowman, B.R., Storz, M.F., 2002. Time series analysis of HASDM thermospheric temperature and density corrections. AIAA 2002–4890, AIAA/AAS Astrodynamics Specialist Conference, Monterey, CA.
- Bowman, B.R., 2004. The semiannual thermospheric density variation from 1970 to 2002 between 200–1100 km. AAS 2004–174, AAS/AIAA Spaceflight Mechanics Meeting, Maui, Hawaii.
- Bowman, B.R., Marcos, F.A., Kendra, M.J., 2004. A method for computing accurate daily atmospheric density values from satellite drag data. AAS 2004–179, AAS/AIAA Spaceflight Mechanics Meeting, Maui, Hawaii.
- Bowman, B.R., Tobiska, W.K., 2006. Improvements in modeling thermospheric densities using new EUV and FUV solar indices. AAS 2006–237, AAS/AIAA Spaceflight Mechanics Meeting, Tampa, FL.
- Bowman, B.R., Tobiska, W.K., Marcos, F., 2006. A new empirical thermospheric density model JB2006 using new solar indices. AIAA 2006–6166, AIAA/AAS Astrodynamics Specialist Conference, Keystone, CO.
- Cook, G.E., 1969. The semi-annual variation in the upper atmosphere: a review. *Annales de Geophysique* 25, 451.
- Jacchia, L.G., 1966. Density variations in the heterosphere. *Annales de Geophysique* 22, 75.
- Jacchia, L.G., 1971a. Semiannual variation in the heterosphere: a reappraisal. *Journal of Geophysical Research* 76, 4602.
- Jacchia, L.G., 1971b. Revised static models of the thermosphere and exosphere with empirical temperature profiles. *Smithsonian Astrophysical Special Report* 332.
- Jacchia, L.G., 1977. Thermospheric temperature, density, and composition: new models. *Smithsonian Astrophysical Special Report* 375.
- Jursa, A.S., 1985. *Handbook of Geophysics and the Space Environment*. Air Force Geophysics Laboratory Air Force Systems Command p. 2–1.
- King-Hele, D.G., Hingston, J., 1968. Air density at heights near 190 km in 1966–7 from the orbit of Secor 6. *Planetary and Space Science* 16, 675.
- McClintock, W.E., Rottman, G.J., Woods, T.N., 2000. SoLar stellar irradiance comparison experiment II (SOLSTICE II) for the NASA earth observing system's solar radiation and climate experiment mission. *SPIE Proceedings* 4135, 225.
- Paetzold, H.K., Zschorner, H., 1961. The Structure of the Upper Atmosphere and its Variations after Satellite Observations, *Space Research II*, 958. North-Holland Publ. Co., Amsterdam.
- Roble, R.G., 1987. Solar cycle variation of the global mean structure of the thermosphere. In: *Proceedings of a Workshop*, November 9–11. The National Center for Atmospheric Research.
- Rottman, G.J., Woods, T.N., 1994. The UARS SOLSTICE. *SPIE Proceedings* 2266, 317.
- Sehnal, L., Vykuttilova, M., Illes, E., Horvath, A., Helali, Y.E., Tawadrous, M.Y., 1988. The semi-annual thermospheric density variation

- between 200–560 km. Bulletin of the Astronomical Institutes of Czechoslovakia 39, 209.
- Storz, M.F., Bowman, B.R., Branson, J.I., 2002. High Accuracy Satellite Drag Model (HASDM). AIAA 2002-4886, AIAA/AAS Astrodynamics Specialist Conference, Monterey, CA.
- Tawadrous, M.Y., 1989. Comparison of observed and modelled semi-annual thermospheric density variations. Bulletin of the Astronomical Institutes of Czechoslovakia 40, 28.
- Viereck, R., Puga, L., McMullin, D., Judge, D., Weber, M., Tobiska, W.K., 2001. The Mg II index: a proxy for solar EUV. Geophysical Research Letters 28 (7), 1342.
- Walker, D.M., 1978. Variations in air density from January 1972 to April 1975 at heights near 200 km. Planetary and Space Science 26, 291.
- Woods, T.N., Rottman, G.J., Roble, R.G., White, O.R., Solomon, S.C., Lawrence, G.M., Lean, J., Tobiska, W.K., 1994. TIMED solar EUV experiment. SPIE Proceedings 2266, 467.